Optics Letters

Simple and fast spectral domain algorithm for quantitative phase imaging of living cells with digital holographic microscopy

Junwei Min,[1,2] Baoli Yao,[2] Steffi Ketelhut,[1] Christian Engwer,[3] Burkhard Greve,[4] and Björn Kemper[1,*]

[1]Biomedical Technology Center, University of Muenster, Mendelstraße 17, D-48149 Muenster, Germany
[2]State Key Laboratory of Transient Optics and Photonics, Xi'an Institute of Optics and Precision Mechanics, Chinese Academy of Sciences, Xi'an 710119, China
[3]Institute for Computational and Applied Mathematics, University of Muenster, Orleans-Ring 10, D-48149 Muenster, Germany
[4]Department of Radiotherapy–Radiooncology, University of Muenster, Albert-Schweitzer Campus 1 Building A1, D-48149 Muenster, Germany
*Corresponding author: bkemper@uni-muenster.de

We present a simple and fast phase aberration compensation method in digital holographic microscopy (DHM) for quantitative phase imaging of living cells. By analyzing the frequency spectrum of an off-axis hologram, phase aberrations can be compensated for automatically without fitting or pre-knowledge of the setup and/or the object. Simple and effective computation makes the method suitable for quantitative online monitoring with highly variable DHM systems. Results from automated quantitative phase imaging of living NIH-3T3 mouse fibroblasts demonstrate the effectiveness and the feasibility of the method. © 2017 Optical Society of America

OCIS codes: (090.1995) Digital holography; (090.1000) Aberration compensation; (180.3170) Interference microscopy; (120.5050) Phase measurement.

https://doi.org/10.1364/OL.42.000227

Digital holographic microscopy (DHM) has been proven to be a powerful tool for noncontact label-free quantitative phase imaging, and has been widely used in various application areas [1–5]. The combination of DHM with conventional optical microscopes simplifies the usage of the technique and makes it convenient to measure different kinds of specimens, as microscope objectives (MOs) can be easily changed while the condenser allows a simple adjustment of the illumination [3,6]. However, the introduction of a condenser and different MOs not only provides high flexibility of illumination and imaging but also causes variable phase aberrations that need to be compensated for in high-resolution quantitative phase imaging.

Many works on the successful compensation of such phase aberrations have already been reported in recent years [5,7–12]. Basically, they can be categorized into physical and numerical compensation techniques. Physical compensation methods introduce the same aberrations into the reference arm to physically counteract the phase aberrations of the object wave, e.g., by using the same optical elements [5,7] or a focus tunable lens [8]. However, adding additional elements not only leads to more complex and expensive systems, but also generates demand for high-precision adjustments in practice. In contrast, numerical compensation methods remove the phase aberrations during the digital reconstruction process with computed phase masks, which are obtained by capturing specimen-free reference holograms [9] or using a numerical fitting of parabolic functions [10], spherical surfaces [11], or Zernike polynomials [12]. Although these methods are known to work well in many situations, they require pre-knowledge about the optical setup or/and the specimen under investigation, and need manual operation steps for recording the reference holograms or selecting a specimen-free area for fitting. These requirements result in inherent drawbacks when methods are applied to DHM setups with highly variable illumination and imaging systems. Manual operations hinder the full automation of the imaging process. Numerical fitting procedures can be sensitive to noise or require additional computational procedures, which sometimes involve additional phase unwrapping steps precluding quantitative online monitoring of fast processes in living cells.

In this Letter, we propose a simple and fast numerical method for quantitative phase imaging of living cells with DHM that is based on the analysis of the spatial frequency spectra of off-axis holograms. Figure 1 shows the flow diagram of our approach. The entire process is based on the typical reconstruction process of off-axis DHM in a spatial frequency domain [4], but does not require pre-knowledge about setup or/and specimen and numerical fitting. By analyzing the spectral orders of the hologram and the retrieved wrapped phase with common image processing algorithms, the parameters for numerical phase masks are detected automatically. The calculated phase masks are then subtracted from the retrieved phase distribution of the object wave to achieve quantitative phase imaging. The whole process is fast and entirely automated.
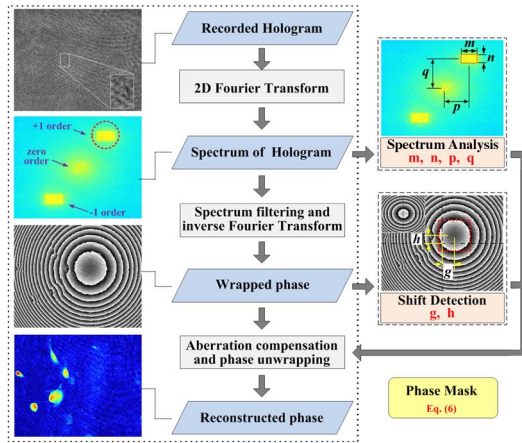
Fig. 1. Entire process of the proposed method. The left block diagrams (dotted box) show the typical reconstruction process of off-axis DHM in spatial frequency domain. The right panels illustrate the additional steps of the proposed algorithm for phase aberration compensation.

The experimental configuration considered in this Letter is depicted in Fig. 2. It consists of a highly variable transmission Mach–Zehnder DHM system that can be combined with common inverted research microscopes [6]. This Letter is based on, but not limited to, this system. The light from a laser is divided by a fiber splitter. After being expanded and collimated, one of the beams passes through the condenser and illuminates the specimen. The condenser generates a homogeneous illumination that can be adapted to the investigated specimens. Moreover, the illumination can be adjusted to be flexible to fit different MOs for the investigation of samples at different magnifications. The light below the specimen is collected by the MO and becomes the spherical object wave O after passing through the tube lens. The other expanded and collimated beam remains unchanged and serves as a plane reference wave R. Its path length and incident angle can be controlled by an optical delay and a mirror M, respectively. The angle between O and R is aligned in such a way that the spatial frequencies of the interference pattern fulfill the *Nyquist* sampling criterion (here: $<3.3°$), and the ±1 spectral orders are separated from the zero order (see Fig. 1). The interference pattern is recorded by a charge coupled device (CCD) camera sensor that is positioned in the image plane.

The inherent phase aberrations of the DHM system basically consist of two contributions. The first is the linear spatial phase shift due to the off-axis tilt of the reference wave.
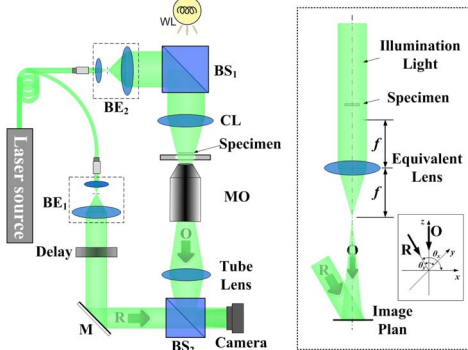
The other one is represented by the spherical phase aberration introduced by a condenser, a MO, and a tube lens. According to the principle of off-axis holography, the linear spatial phase shift can be described as $\varphi_t(x, y) = k_x x + k_y y$, where $k_x = 2 \sin(\theta_x/2)/\lambda$, $k_y = 2 \sin(\theta_y/2)/\lambda$ are the spatial carrier frequencies of the off-axis hologram that indicate the shift of the ±1 order side bands from the center of the spectrum. The parameters θ_x and θ_y are the angles between R and the optical axis perpendicular to the CCD sensor plane, respectively, as shown in the inset of Fig. 2. The wavelength of the applied laser light is represented by λ, and the effective magnification of the optical imaging system is assumed to A. M and N are the pixel numbers of the camera sensor in the x and y directions, and px and py denote the CCD pixel dimensions. Hence, the area of the recorded hologram is $W_c \times H_c$, where $W_c = M \times px$ and $H_c = N \times py$. The corresponding sampling intervals along the horizontal and vertical directions in the spatial frequency domain are $1/W_c$ and $1/H_c$, respectively. We can measure the distances p and q of the center of the $+1$ spectral order to the center of the spectrum of an off-axis hologram, as shown in Figs. 1 and 3. The corresponding numerical phase mask for the compensation of the linear phase change in the object plane is

$$\varphi_t(x, y) = \frac{p}{A^2}x + \frac{q}{A^2}y. \tag{1}$$

The spherical phase aberration induced by the optical imaging system can be described by $\varphi_s(x, y) = \cdot (x^2 + y^2)/r$, where r is the radius relative to the focal length of the lenses and their interjacent distances [13]. In practice, the aberrations induced by the imaging system are much larger than the phase changes caused by samples with low spatial phase variations such as most biological cells and coherence-induced disturbances, e.g., induced by multiple reflections within the optical setup. Thus, the spatial frequency spectrum of a hologram is predominated by the off-axis tilt and spherical phase aberrations. Figure 3(a) shows an off-axis hologram of living NIH-3T3 mouse fibroblasts that was recorded with a setup, as shown in Fig. 2, using a $10 \times$ MO (NA $= 0.3$), while Fig. 3(b) depicts an according specimen free hologram that was recorded under the same imaging conditions. Figures 3(c) and 3(d) present spectra corresponding to Figs. 3(a) and 3(b), respectively, with the according spectral coordinates ξ
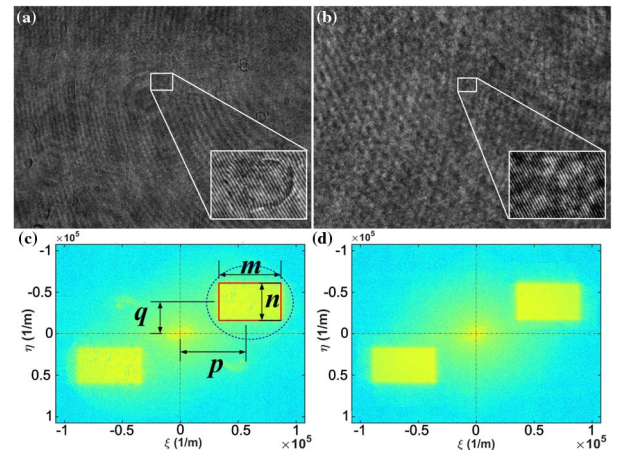

Fig. 2. Schematic of the experimental setup for DHM. WL, white light source; BE1/BE2, beam expenders; BS1/BS2, nonpolarizing beam splitters; CL, condenser lens; MO, microscope objective; M, mirror.

Fig. 3. (a) Off-axis hologram of living NIH-3T3 mouse fibroblasts and (b) specimen free off-axis hologram utilizing the same imaging conditions as in (a); (c), (d) spectra of (a) and (b), respectively.

and η. The presence of the cells affects only the inner distribution of the ± 1 order side bands, while their size depends on the spatial frequencies caused by the spherical aberrations which are induced by the entire imaging system, as well as by the size and aspect ratio of the CCD sensor. In Fig. 3(c), we can locate the coordinates p, q of the center of the $+1$ order side band and measure its size to $m \times n$. Based on the principles of geometric optics, we can use a single equivalent lens with a focal length f to describe the whole imaging system in the object arm as shown in the right block diagram in Fig. 2. The spherical phase aberration thus can be rewritten as $\varphi_s(x,y) = (x^2 + y^2)/f$. According to the properties of the single lens [4,14], the relations between side band size, sensor dimensions, and imaged field of view are

$$m = \frac{W_i}{\lambda f}, \qquad n = \frac{H_i}{\lambda f}, \qquad (2)$$

where $W_i = W_c/A$, $H_i = H_c/A$. The product $W_i \times H_i$ represents the imaged field of view in the object plane. Hence, as shown in Eq. (2), the corresponding focal length of the equivalent lens can be calculated from the $+1$ side band size in either the x or y direction:

$$f_x = \frac{W_c}{A\lambda m}, \qquad f_y = \frac{H_c}{A\lambda n}, \qquad (3)$$

where $f_x = f_y = f$. To clarify the contributions of the parameters m, n to the phase mask for compensation of spherical phase aberrations, we use the relation $f = f_x = f_y$ and get

$$\varphi_s(x,y) = x^2/f_x + y^2/f_y = \frac{A\lambda m}{W_c} x^2 + \frac{A\lambda n}{H_c} y^2. \qquad (4)$$

In an ideal situation, after the compensation of the phase shift, due to the off-axis tilt, the center of the retrieved circular wrapped phase pattern that is caused by spherical aberrations should be located in the center of the field of view (the small image in the inset "shift detection" of Fig. 1). However, errors during the detection of the parameters p and q may cause a slight relative shift to the center of the field of view. We can measure this shift by the determination of the parameters g and h along the horizontal and vertical directions in the tilt compensated wrapped phase map (the inset "shift detection" of Fig. 1) and consider it in a revised version of Eq. (4):

$$\varphi_s'(x,y) = \frac{A\lambda m}{W_c}(x-g)^2 + \frac{A\lambda n}{H_c}(y-h)^2. \qquad (5)$$

The addition of Eqs. (1) and (5) yields the final numerical phase mask for the compensation of both off-axis tilt and spherical aberrations:

$$\varphi_{tot}(x,y) = \varphi_s'(x,y) + \varphi_t(x,y)$$
$$= \frac{A\lambda m}{W_c}(x-g)^2 + \frac{A\lambda n}{H_c}(y-h)^2 + \frac{p}{A^2}x + \frac{q}{A^2}y. \qquad (6)$$

To reduce the computational amount for online monitoring, it is sufficient to perform the spectrum analysis and shift detection within the spatial filtered part of the spectrum (dotted circle in the right inset of Fig. 1) and in a cropped continuous region of the wrapped phase map (red dotted box in the right inset of Fig. 1).

To verify the feasibility and effectiveness of the proposed method, we applied it for quantitative phase imaging of living NIH-3T3 mouse fibroblasts. The cells are grown on a structured collagen surface and are observed inside a Petri dish filled with cell culture medium. For imaging, an experimental

setup, as shown in Fig. 2, was used. The laser light wavelength was $\lambda = 532$ nm. A CCD sensor with 1280×960 pixels and a pixel size of 4.65×4.65 µm was utilized for hologram recording. We first used a $10\times$ MO (NA = 0.3) to locate the specimens. Figure 4(a) displays the recorded digital off-axis hologram. The enlarged area shows a part of the carrier fringes superimposed with a diffraction pattern caused by a living NIH-3T3 cell. Figure 4(c) depicts the corresponding frequency spectrum of the recorded hologram. We can measure the distances between the center of the $+1$ order side band and the zero order to $p = 0.66 \times 10^5$ m^{-1} and $q = 0.39 \times 10^5$ m^{-1}, respectively, by using the object analysis functions of the MATLAB image processing toolbox. The blue dotted circle in Fig. 4(c) indicates the applied spectral filter that separates the $+1$ order side band during the reconstruction process. Within the selected circular part of the spectrum, the size $m \times n$ of the $+1$ order side band was determined to be 0.55×0.41 ($\times 10^5$ m^{-1})^2. Figure 4(e) shows the resulting wrapped phase that was retrieved after spatial filtering, centering of the spectrum according to the parameters p and q, and application of an inverse Fourier transform. A small remaining lateral shift of the circular pattern from the center of the field of view due to localization errors is observed. We can use the centroid analysis function of the image processing toolbox of MATLAB to
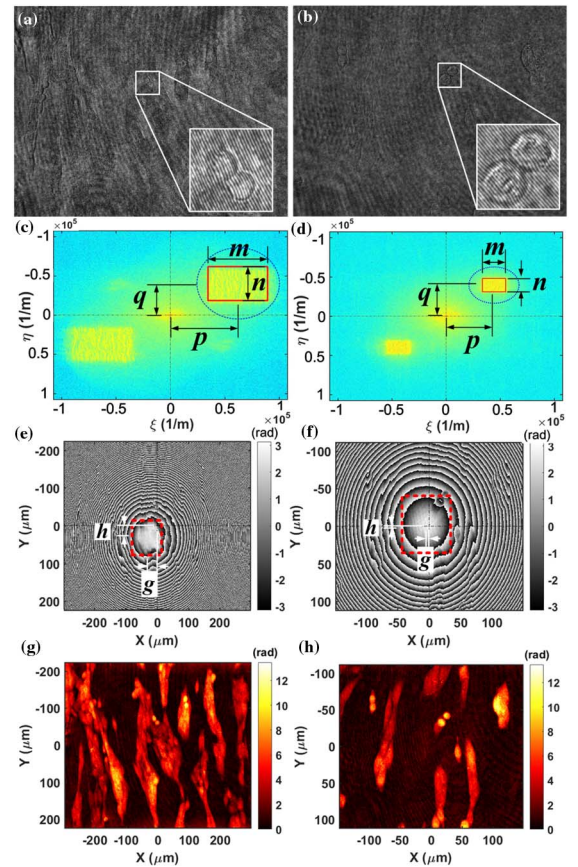

Fig. 4. Quantitative phase imaging of living NIH-3T3 mouse fibroblasts. (a) Off-axis hologram recorded with a 10× MO and (b) off-axis hologram recorded with a 20× MO; (c), (d) spectra of (a) and (b); (e), (f) wrapped phase maps reconstructed from (c) and (d) after off-axis tilt compensation; (g), (h) corresponding reconstructed quantitative phase images after compensation of phase aberrations with Eq. (6), considering the parameters g and h.

measure this shift along the x and y direction with subpixel accuracy and get $g = 32.43$ μm and $h = 41.82$ μm, respectively, within the cropped continuous region that is indicated in Fig. 4(e) by the dotted red box. Excluding the computational time for spectrum centering and the inverse Fourier transform, the duration for spectral analysis and shift detection was measured to 7.3 ms (computer with Intel Core i5 CPU, 2.50 GHz). Inserting all retrieved parameters p, q, m, n, g, and h into Eq. (6) for phase aberration compensation, the final quantitative phase image of the cellular specimens is retrieved after unwrapping [Fig. 4(g)]. Spherical phase aberrations and off-axis tilt appear to be eliminated, while the cells become visible with a high contrast on a plain phase background with spatial phase variations <1.4 rad within the field of view.

After localization, the cells were analyzed in a time-lapse observation experiment. Therefore, the magnification of the MO was changed to 20 × (NA = 0.4), and the condenser was realigned, respectively. In order to image cellular growth and migration dynamically, digital off-axis holograms were recorded every 3 min during a period of 16 h and, subsequently, evaluated with the proposed method. Figures 4(b) and 4(d) show a representative recorded off-hologram and its frequency spectrum. The corresponding retrieved wrapped phase map is displayed in Fig. 4(f). The comparison with the results from the 10x MO, shows that the spectrum size is inversely proportional to the magnification [Figs. 4(c) and 4(d)], while a smaller shift due to detection errors occurs [Figs. 4(e) and 4(f)]. Following the same procedures for spectrum analysis and shift detection as above, the parameters m, n, p, q, g, and h for the 20 × objective were determined to be 0.22×10^5 m^{-1}, 0.17×10^5 m^{-1}, 0.45×10^5 m^{-1}, 0.39×10^5 m^{-1}, 4.92 μm, and 3.48 μm, respectively. Figure 4(h) shows the final reconstructed quantitative phase image of the specimens after phase aberration compensation with Eq. (6) and phase unwrapping. Both tilt and spherical aberrations are removed successfully, and the retrieved quantitative phase image appears with a flat background. The corresponding spatial phase variations are determined to be <1 rad.

Figure 5 illustrates the further evaluation of the recorded hologram series. Figure 5(a) shows a recorded off-axis hologram. The red box in Fig. 5(b) labels the automated detected location and size of the +1 order side band for the retrieval of the parameters p, q and m, n in the according spectrum. Figures 5(c) and 5(d) show the reconstructed quantitative phase image after phase aberration compensation and a corresponding pseudo 3D view that illustrates the achieved flatness of the phase background. Visualization 1 demonstrates the automated evaluation of all 300 off-axis holograms by a fast motion movie. Both the size of the +1 side band and its off-axis shift are detected with high reliability in each hologram. In the retrieved series of the quantitative phase images, it becomes visible that the cells divide, migrate, and change their alignment.

In summary, we have presented a simple and fast phase aberration compensation method for quantitative phase imaging of living cells that is suitable, in particular, for DHM configurations with highly variable illumination and imaging systems. By detecting the position and size of the +1 spectral order, linear and spherical phase aberrations can be compensated for automatically without any manual operation or pre-knowledge of the setup or/and the object. The entire process does not require numerical fitting and is insensitive to coherence-induced noise that is distributed as a homogeneous background in the spectral domain. Quantitative phase imaging of living NIH-3T3 mouse fibroblasts demonstrates the performance and the robustness of the principle. Although the application of our method is limited to thin phase objects such as biological cells, it prospects various applications in the fields of nondestructive testing, e.g., surface inspection [3,4] or residual stress measurements [15], and in biomedicine, including in particular simplified quantitative online monitoring of living cells in an automated manner.

Fig. 5. Online monitoring of living NIH-3T3 mouse fibroblasts. (a) Recorded off-axis hologram, (b) frequency spectrum of (a), (c) reconstructed quantitative phase image after phase aberration compensation utilizing the proposed method, and (d) pseudo 3D view of (c). Visualization 1 shows a fast motion movie of the whole observation period of 16 h.

REFERENCES

1. E. Cuche, F. Bevilacqua, and C. Depeursinge, Opt. Lett. **24**, 291 (1999).
2. G. Pedrini, S. Schedin, and H. Tiziani, J. Mod. Opt. **47**, 1447 (2000).
3. B. Kemper and G. Bally, Appl. Opt. **47**, A53 (2008).
4. M. Kim, *Digital Holographic Microscopy: Principles, Techniques, and Applications* (Springer, 2011).
5. P. Girshovitz and N. T. Shaked, Biomed. Opt. Express **3**, 1757 (2012).
6. B. Kemper, D. Carl, A. Höink, G. von Bally, I. Bredebusch, and J. Schnekenburger, Proc. SPIE **6191**, 61910T (2006).
7. W. Qu, C. Chee, Y. Yu, and A. Asundi, Opt. Lett. **34**, 1276 (2009).
8. A. Doblas, D. Hincapie-Zuluaga, G. Saavedra, M. Martínez-Corral, and J. Garcia-Sucerquia, Appl. Opt. **54**, 5229 (2015).
9. P. Ferraro, S. Nicola, A. Finizio, G. Coppola, S. Grilli, C. Magro, and G. Pierattini, Appl. Opt. **42**, 1938 (2003).
10. C. Zuo, Q. Chen, W. Qu, and A. Asundi, Opt. Lett. **38**, 1724 (2013).
11. J. Di, J. Zhao, W. Sun, H. Jiang, and X. Yan, Opt. Commun. **282**, 3873 (2009).
12. T. Colomb, F. Montfort, J. Kühn, N. Aspert, E. Cuche, A. Marian, F. Charrière, S. Bourquin, P. Marquet, and C. Depeursinge, J. Opt. Soc. Am. A **23**, 3177 (2006).
13. J. Min, B. Yao, P. Gao, B. Ma, S. Yan, F. Peng, J. Zheng, T. Ye, and R. Rupp, Optik **123**, 1525 (2012).
14. J. Goodman, *Introduction to Fourier Optics* (Roberts & Company, 2005).
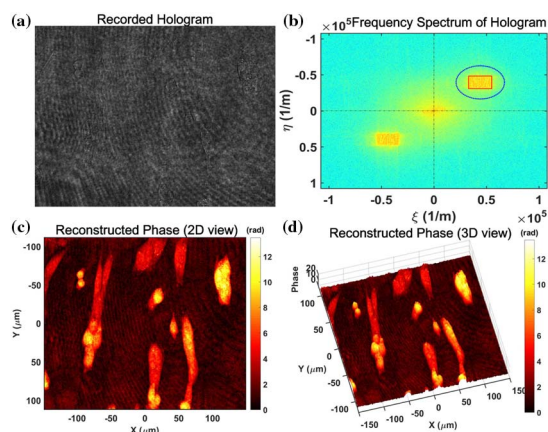15. X. Huang, Z. Lui, and H. Xie, Acta Mech. Solida Sin. **26**, 570 (2013).